

# Heat Flow in Fractured Rocks: Stress and Moisture-Dependent Thermal Contact Resistance

A.V. Garcia<sup>\*</sup>, J.C. Santamarina

KAUST, Physical Sciences and Engineering, Thuwal, 23955-6900, Saudi Arabia

## ABSTRACT

The thermal conductivity of fractured rock masses is an important parameter for the analysis of energy geosystems, yet, its measurement is challenged by specimen size requirements. Fluids within fractures have lower thermal conductivities than rock minerals and heat flow lines constrict through contacting asperities. Together, heat flow constriction and phonon boundary scattering cause an apparent temperature discontinuity across the fracture, typically represented as a thermal contact resistance. We investigate the thermal contact resistance in fractured limestone and its evolution during loading and unloading ( $\sigma' = 10$  kPa to  $\sigma' = 3000$  kPa) for clean and gouge-filled fractures, under both air-dry and water-saturated conditions. The fracture thermal contact resistance decreases during loading because of the increase in the true contact area, gouge and asperity crushing, and fracture filling by produced fines that contribute new conduction pathways. These processes convey high stress sensitivity and loading hysteresis to the fracture thermal contact resistance. Water fills the fracture interstices and forms menisci at mineral contacts that significantly improve heat conduction even in partially saturated rock masses. The rock mass effective thermal conductivity can be estimated by combining the intact rock thermal conductivity with measurements of the thermal contact resistance of a single fracture under field boundary conditions.

## 1. Introduction

The thermal conductivity of fractured rock masses is an important parameter for the analysis of hydrothermal aquifers (Pasvanoğlu 2020), hot dry rock geothermal systems (Brown et al. 2012), deep borehole heat exchangers (Laloui et al. 2006, Bär et al. 2015, Welsch et al. 2016), nuclear waste disposal sites (Tsang 2012, Madsen 1998), and some oil and gas operations (Stephens and Voight 1982, Wang and Dusseault 2003).

The thermal conductivity of intact rocks increases with effective stress due to microcrack closure (Bridgman 1924; Hurtig and Brugger 1970, Walsh and Decker 1966, Clauser and Huenges 1995, Abdulagatov et al. 2006, Abdulagatova et al. 2009, Abdulagatova et al. 2010, Alishaev et al. 2012). Conversely, differential thermal expansion amongst adjacent crystals in the rock matrix can lead to thermally induced cracking and a decrease of thermal conductivity with temperature (Clauser and Huenges 1995, Abdulagatov et al. 2006, Abdulagatova et al. 2009, Abdulagatova et al. 2010, Alishaev et al. 2012).

Fluids have lower thermal conductivities than rock minerals ( $k_w = 0.6$  W.m<sup>-1</sup>.K<sup>-1</sup> for water and  $k_a = 0.024$  W.m<sup>-1</sup>.K<sup>-1</sup> for air, while  $k_m = 1$  to 10 W.m<sup>-1</sup>.K<sup>-1</sup> for minerals – Lide, 2003). Therefore, when thermal energy flows across a fracture, heat flow lines constrict through contacting asperities. In addition, narrow asperities resist heat flow due to the boundary scattering of phonons (Prasher et al., 2007; Prasher and

Phelan, 2006). Together, heat flow constriction and phonon boundary scattering cause an apparent temperature discontinuity  $\Delta T_c$  across the fracture (Figure 1). We define the thermal contact resistance  $R_c$  [m<sup>2</sup>.K.W<sup>-1</sup>] as the ratio between the temperature drop  $\Delta T_c$  [K] and the heat flux  $q_c$  [W.m<sup>-2</sup>] across a fracture.

$$R_c = \frac{\Delta T_c}{q_c} \quad (1)$$

Current thermal contact resistance models consider the effects of stress, the contact geometry, and mechanical properties, and the thermal properties of the interstitial fluids at contacting surfaces (Cooper et al. 1969, Mikić 1974, Yovanovich 2005). However, models fail to recognize the effect of evolving contacts and the presence of gouge in rock fractures.

In fact, data gathered using high spatial resolution techniques (laser heat source and infrared radiometer – Popov et al. 1999, Surma and Geraud 2003) show that mechanical damage reduces rock thermal conductivity (Li et al. 2020), and the presence of fractures hinders the upscaling of local measurements to determine the effective thermal conductivity of the rock mass (Jorand et al. 2013).

Despite the importance of fractures to thermal conductivity, the thermal contact resistance of rock fractures remains poorly studied; in addition, the measurement of the effective thermal conductivity of rock masses is challenged by specimen size requirements. This paper presents

<sup>\*</sup> Corresponding author.

E-mail address: [adrian.garcia@kaust.edu.sa](mailto:adrian.garcia@kaust.edu.sa) (A.V. Garcia).

an experimental study of the thermal contact resistance in fractured limestone and its evolution for various fracture conditions. Then, we upscale thermal contact resistance trends to predict the rock mass effective thermal conductivity and compare predictions with experimental results.

## 2. Experimental design: materials, devices and procedure

### 2.1. Materials

The tested specimens consist of stacked Jordanian limestone slabs (15 cm × 15 cm × 4 cm – Figure 2) to render a fracture density of 25 fractures per meter. This is a predominantly calcite rock (confirmed by XRD analysis), and it has a thermal conductivity that ranges from 2.83 W.m<sup>-1</sup>.K<sup>-1</sup> to 3.05 W.m<sup>-1</sup>.K<sup>-1</sup>, which is consistent with low porosity limestones (Yaşar et al. 2008).

The selected gouge is a carbonate sand #40-60 with similar mechanical and thermal properties as the limestone slabs. We use thresholded microscopic images of the gouge material to measure minimum Feret diameters and the volume of each grain to compute the grain size distribution. Prior to loading, the sand exhibits a Gaussian distribution with a mean grain size of  $\mu = 0.39$  mm and a standard deviation of  $sd = 0.05$  mm (Figure 3-a).

Both clean and gouge-filled fractures are tested under air-dry and water-saturated conditions (Figure 2-a). We polish each limestone slab with 120 grit sandpaper to ensure a planar surface of consistent roughness. Gouge-filled fractures receive a monolayer of the carbonate sand. The preparation of the water-saturated specimens involves the same polishing and gouge placement procedure but within a thin plastic liner that we later fill with water and seal to prevent evaporation.

### 2.2. Instrumentation

Thermocouples are inserted in drilled holes (3 mm diameter, 7.5 cm deep, and 5 mm away from the fracture surfaces) to reach the vertical central axis of the specimen for precise measurements of internal temperatures through time (Figure 2-b). We extrapolate the linear thermal gradient between the two thermocouples in each limestone slab to the slab surfaces in order to determine the temperature discontinuity across the fractures.

Temperature data time averaging (about 400 measurements) reduces random fluctuations to a precision better than  $\varepsilon_T = 0.01^\circ\text{C}$ . Albeit low, this uncertainty hinders the accurate determination of the thermal contact resistance  $R_c$ . We therefore conducted two sets of tests. Effective thermal conductivity measurements are based on a stack of five limestone slabs. Whereas, thermal contact resistance measurements only use

two slabs to increase the thermal gradient and obtain higher precision in  $R_c$ -measurements; in the two-slab configuration, the error  $\varepsilon_T$  divided by the temperature drop across the fracture  $\Delta T$  is  $\varepsilon_T/\Delta T \approx 0.04$ .

### 2.3. Thermal boundaries and heat flux

We place heat exchange steel plates on both ends of the stacked slabs and feed them with two separate temperature-controlled circulators (VersaCool – Figure 2-a). We set the top plate at  $90^\circ\text{C}$  and the lower plate at  $10^\circ\text{C}$ . The top-to-bottom thermal gradient mitigates peripheral thermal convection effects. Additionally, a 5 cm thick Styrofoam insulation surrounds the specimen to minimize heat loss. Two- and five-slab configurations have the same setup and boundary conditions. In both cases, we measure the thermal heat flux with a calibrated acrylic plate ( $k = 0.21$  W.m<sup>-1</sup>.K<sup>-1</sup>) placed in series between the top heat plate and the rock specimen (Figure 2-b). All temperature measurements are made under steady-state conditions.

### 2.4. Mechanical load

The limestone stack held between the two heat exchange plates sits within a rigid reaction frame that imposes preselected effective stress levels between  $\sigma' = 10$  kPa and  $\sigma' = 3000$  kPa following a stress increment ratio of 3. A side-mounted LVDT monitors the specimen global deformation.

Figure 4 shows a complete set of temperature signatures gathered during loading and unloading of the air-dry, gouge-filled limestone specimen. The test lasts 190 hours so that steady-state thermal conditions are reached after each load step. The first ten hours show the temperature evolution after starting the circulators, so that the higher slabs heat up while the lower slabs become cooler. The heat flux through the acrylic plate is equal to the heat transported through the rock stack  $Q_{\text{rock}} = Q_{\text{acry}}$ , therefore:

$$\frac{\Delta T_{\text{rock}}/L_{\text{rock}}}{\Delta T_{\text{acry}}/L_{\text{acry}}} = \frac{k_{\text{acry}}}{k_{\text{rock}}} \quad (2)$$

The relatively low thermal conductivity in the acrylic plate allows for accurate flux determinations and limits the thermal gradient in the rock  $\Delta T_{\text{rock}}/L_{\text{rock}}$ . Equation 2 helps explain notable features in the data shown in Figure 4, such as: (1) the effective thermal range across the rock stack is  $13^\circ\text{C}$  to  $35^\circ\text{C}$ , compared to the applied  $10^\circ\text{C}$  to  $90^\circ\text{C}$  range; (2) there is an initial overcooling of the lower slabs because the initial heat conduction is faster towards the cooler lower heat exchanger as there is no acrylic plate at the bottom; and (3) as the thermal conductivity in the rock mass  $k_{\text{rock}}$  increases with normal stress, the temperature range across the rock mass decreases,  $\Delta T_{\text{rock}}/L_{\text{rock}}$ .

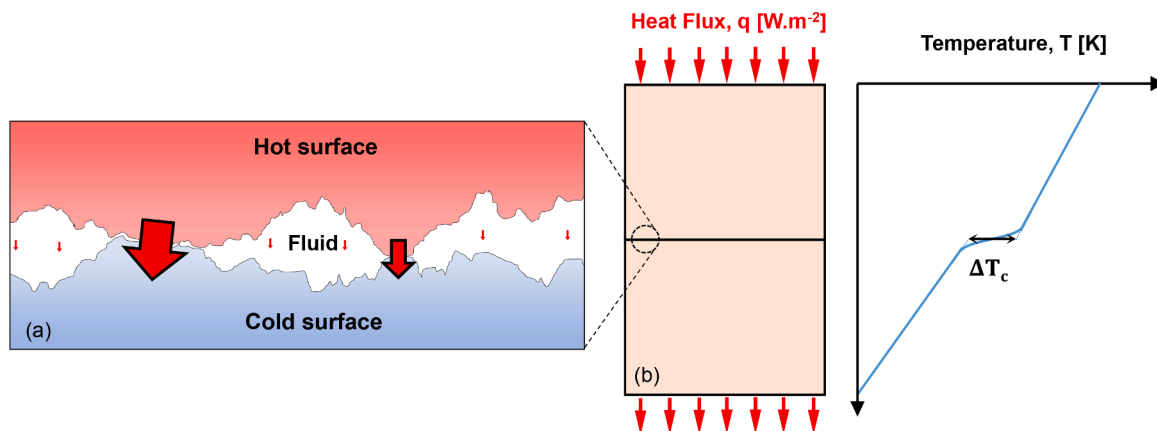


**Figure 1.** Thermal contact resistance. (a) Heat flow constriction through contacting asperities. (b) Macroscopically apparent temperature discontinuity at the contact.

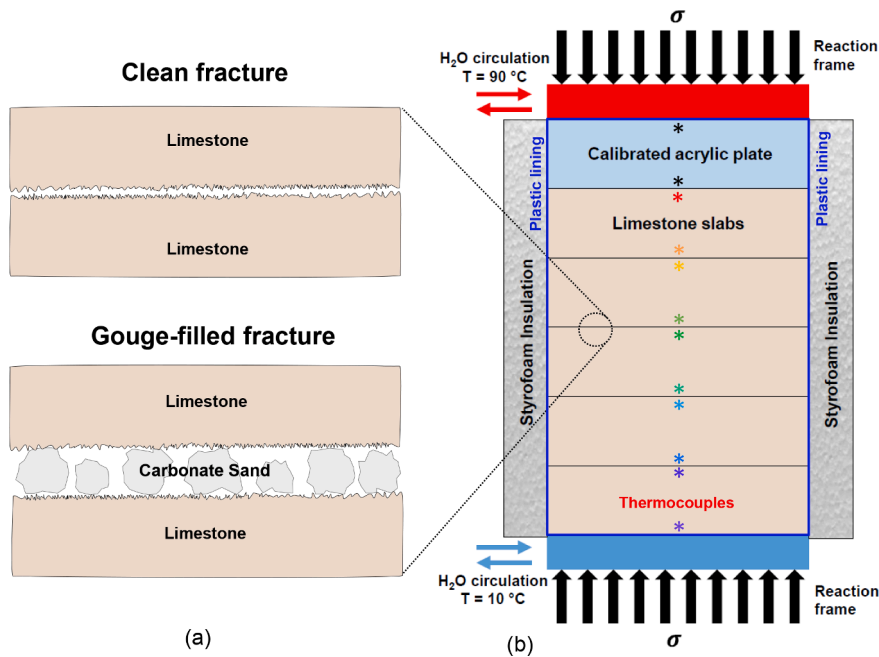


Figure 2. Experimental device and fracture interstitial conditions. (a) Clean and gouge-filled fractures – tested under dry and water saturated conditions. (b) Stress-controlled thermal measurement system for fractured rock.

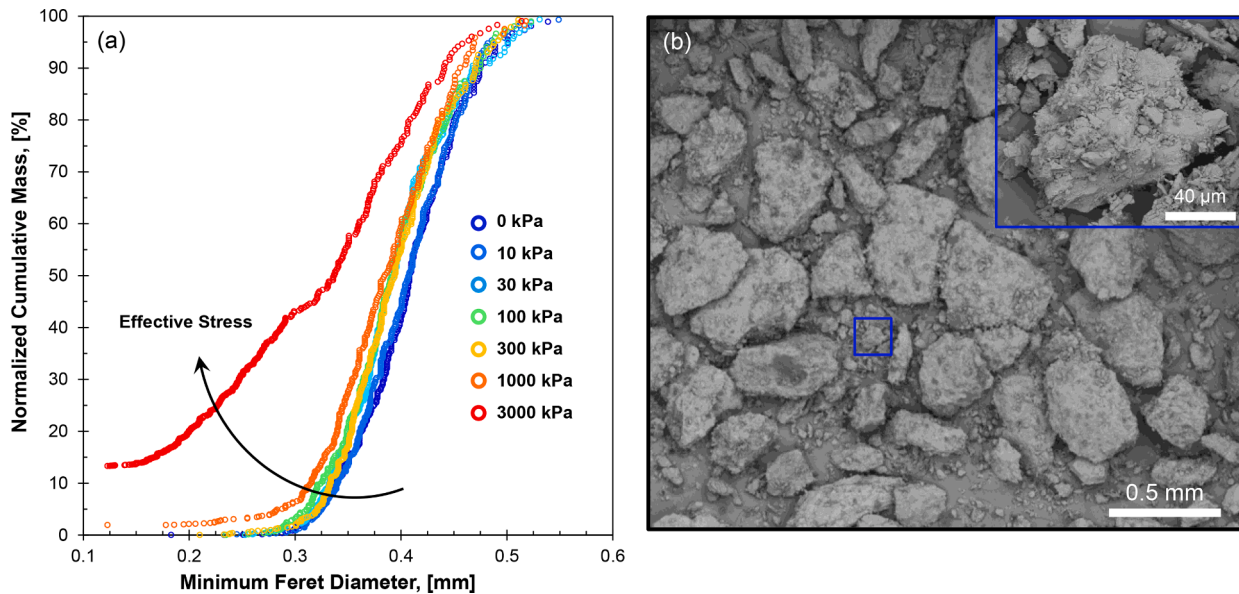


Figure 3. Fracture gouge: carbonate sand. (a) Grainsize distributions of air-dry gouge specimens subjected to various stress levels. (b) Scanning electron microscopic image of gouge after 3 MPa loading under water-saturated conditions.

### 3. Experimental Results

#### 3.1. Five-slab Stacks

Figure 5 presents the flux-normalized temperature gradient (i.e., thermal resistance) through clean and gouge-filled fractured limestone specimens for both air-dry and water-saturated conditions; for clarity, data corresponds to the extreme effective stresses,  $\sigma' = 10\text{ kPa}$  and  $\sigma' = 3000\text{ kPa}$ . The overall slope is the effective conductivity  $k_{eff}$  of the rock mass, whereas the local slope for each slab represents the thermal conductivity  $k_m$  of the intact limestone. The temperature discontinuities define the thermal contact resistance  $R_c = \Delta T_c/q$  at each fracture.

Data show that the presence of carbonate gouge increases the contact

resistance in both dry and water-saturated specimens, and makes the contact resistance more sensitive to stress than in clean fractures. Water saturation reduces the thermal contact resistance and increases the effective thermal conductivity, particularly in gouge-filled fractures at low stress.

Figure 6 depicts the vertical load-deformation divided by the number of fractures during loading and unloading for both clean and carbonate gouge-filled fractures under air-dry and water saturated conditions. Clean, air-dry fractures (Figure 6-a) exhibit the smallest shortening, and there is a relatively minor permanent deformation upon unloading. The presence of gouge within fractures increases the specimen shortening during loading and the permanent deformation after unloading for both dry and wet conditions (Figures 6-b-and-d). Water-saturation enhances

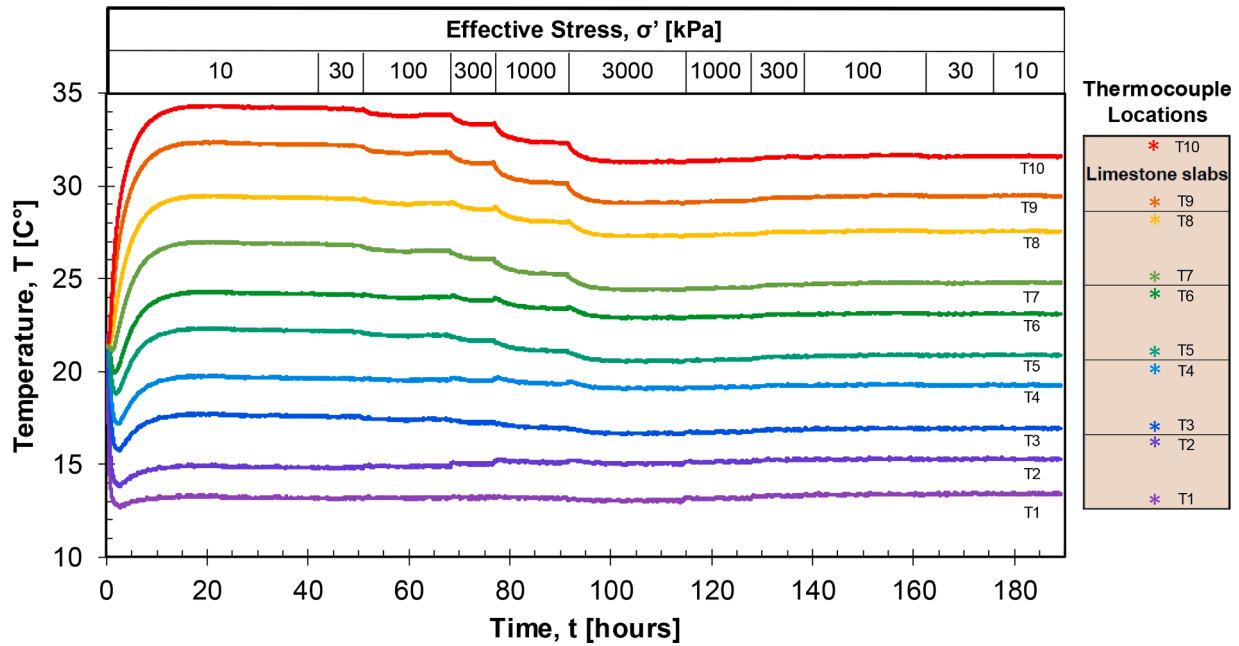


Figure 4. Typical thermocouple temperature-time signatures. Data for an air-dry gouge-filled limestone specimen during loading and unloading. Color-pairs correspond to the two thermocouples in each of the 5 slabs (refer to Figure 2).

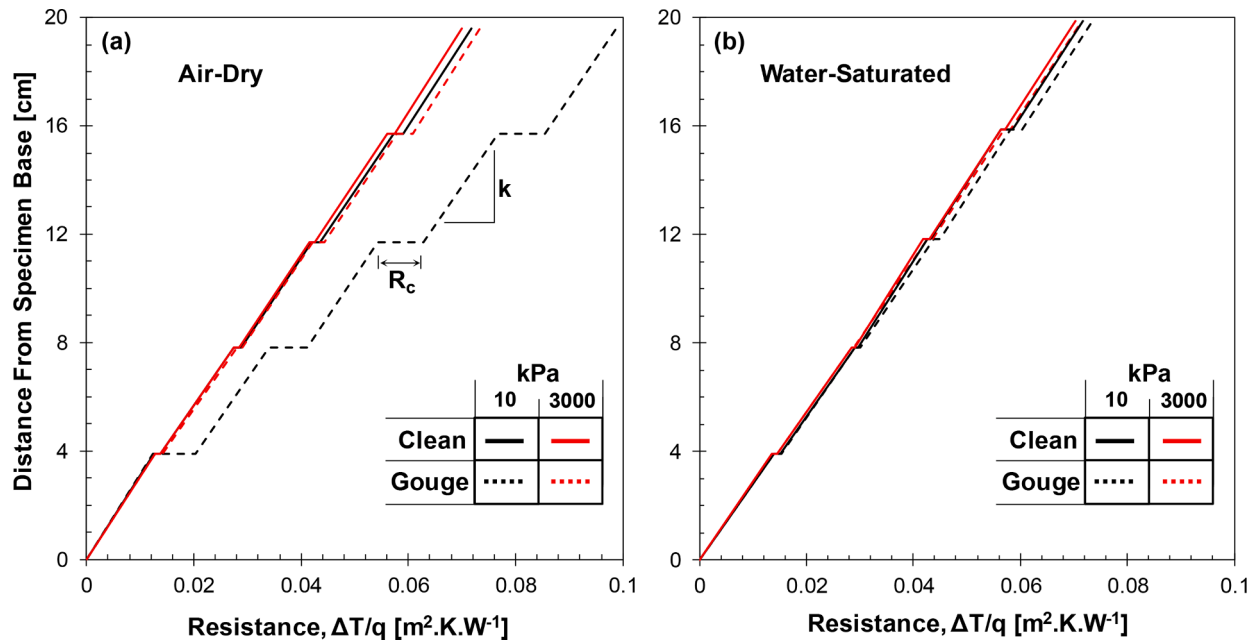


Figure 5. Specimen height vs. resistance across a five-slabs stack (a) Dry and (b) water-saturated specimens. Data shown for clean and gouge-filled fractures under the low and high effective stresses ( $\sigma' = 10$  kPa and  $\sigma' = 3000$  kPa).

shortening and hysteresis; in fact the wet, gouge-filled fractured specimen shortened the most.

Global deformation measurements are consistent with gouge crushing. Figure 3-a plots the normalized cumulative mass of the air-dry carbonate gouge against the minimum particle Feret diameters for various specimens subjected to different effective stress levels from  $\sigma' = 0$  kPa to  $\sigma' = 3000$  kPa. The grainsize distribution of the gouge material changes significantly when the normal stress exceeds  $\sigma' = 1000$  kPa. Figure 3-b shows an SEM image of gouge after loading to  $\sigma' = 3000$  kPa under water-saturated conditions. The particles range from sub-micron to half a millimeter in size and are highly angular indicating extensive crushing. Small grains cling to large grains and cluster at contacts

because of capillary forces experienced during oven drying. The presence of water exacerbates particle crushing and fines generation (Figure 3-b – see similar observations and underlying fracture mechanical analysis in Oldecop and Alonso 2001).

### 3.2. Two-slab Stacks

Figures 7-a-and-b show the fracture thermal contact resistance computed from the thermal discontinuities measured for clean and gouge-filled fractures under dry and water-saturated conditions during loading and unloading. These tests involve two-slab stacks with a single fracture to obtain high resolution measurements of contact resistance.

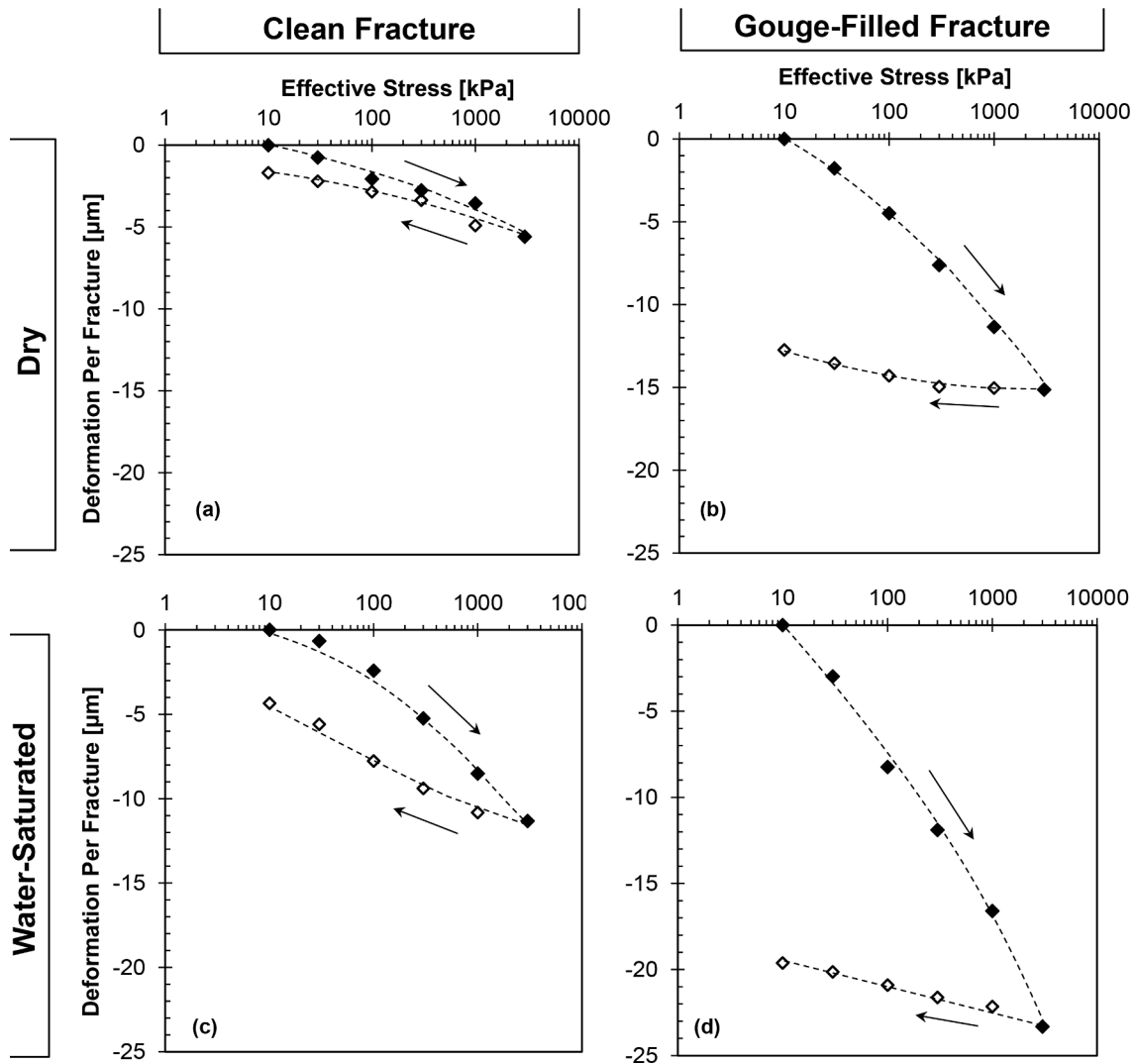


Figure 6. Deformation versus effective stress during loading and unloading - Five-slabs stacks. Clean fractures (a & b) and carbonate gouge-filled fractures (c & d) under dry and water saturated conditions.

The thermal contact resistance of gouge-filled fractures is very sensitive to stress during virgin loading and displays a prominent hysteresis upon unloading. Hysteresis is less conspicuous in clean fractures. Water saturation significantly reduces thermal contact resistance all cases.

#### 4. Discussion and Analysis

##### 4.1. Fracture Thermal Contact Resistance

Experimental results show that the thermal contact resistance depends strongly upon the applied normal stress and interstitial conditions such as the presence of gouge and water saturation. For dry fractures, the true mineral-to-mineral contact area relates to the effective stress in accordance with contact mechanics (Greenwood and Williamson 1966). In the limit of rigid-plastic media, the true contact area  $a_c$  relates to the apparent area  $a_a$  as the ratio between the applied stress  $\sigma$  to the yield stress  $\sigma_y$ ,  $a_c/a_a = \sigma/\sigma_y$ . Furthermore, asperities and gouge experience crushing at high loads; gradually, fines fill the voids in fractures, provide additional conduction pathways, and enhance the heat flow across the fracture (Yun and Santamarina 2008). Therefore, hysteresis in thermal contact resistance is more prominent in gouge-filled fractures than in clean fractures, as observed in experimental results (Figure 7).

A contact mechanics-inspired power function adequately fits the

inverse relationship between the measured thermal contact resistance  $R_c$  and the normal effective stress  $\sigma'$  (Figure 7):

$$R_c = R_{cL} \left( \frac{\sigma' + \sigma'_0}{\sigma'_0} \right)^{-\beta} \tag{3}$$

where  $R_{cL}$  is the asymptotic thermal contact resistance when the applied stress  $\sigma'$  is much smaller than the characteristic effective stress  $\sigma' \ll \sigma'_0$ . Table 1 lists the  $R_{cL}$ ,  $\sigma_0$ , and  $\beta$  values used to fit the thermal contact resistance data in Figure 7.

The presence of water can reduce thermal contact resistance by nearly 70% for clean or gouge-filled fractures. While water has lower thermal conductivity than the rock mineral, its thermal conductivity is 25-times that of air. Therefore, even a small amount of water in the contact interstices and in menisci at mineral contacts can profoundly reduce the fracture thermal contact resistance.

##### 4.2. Rock Mass Effective Thermal Conductivity – Upscaling

The fracture thermal response strongly affects the rock mass thermal conductivity. Figure 8-a depicts the measured effective thermal conductivity for five-slab limestone specimens with four clean and gouge-filled fractures under dry and water-saturated conditions, during loading and unloading.

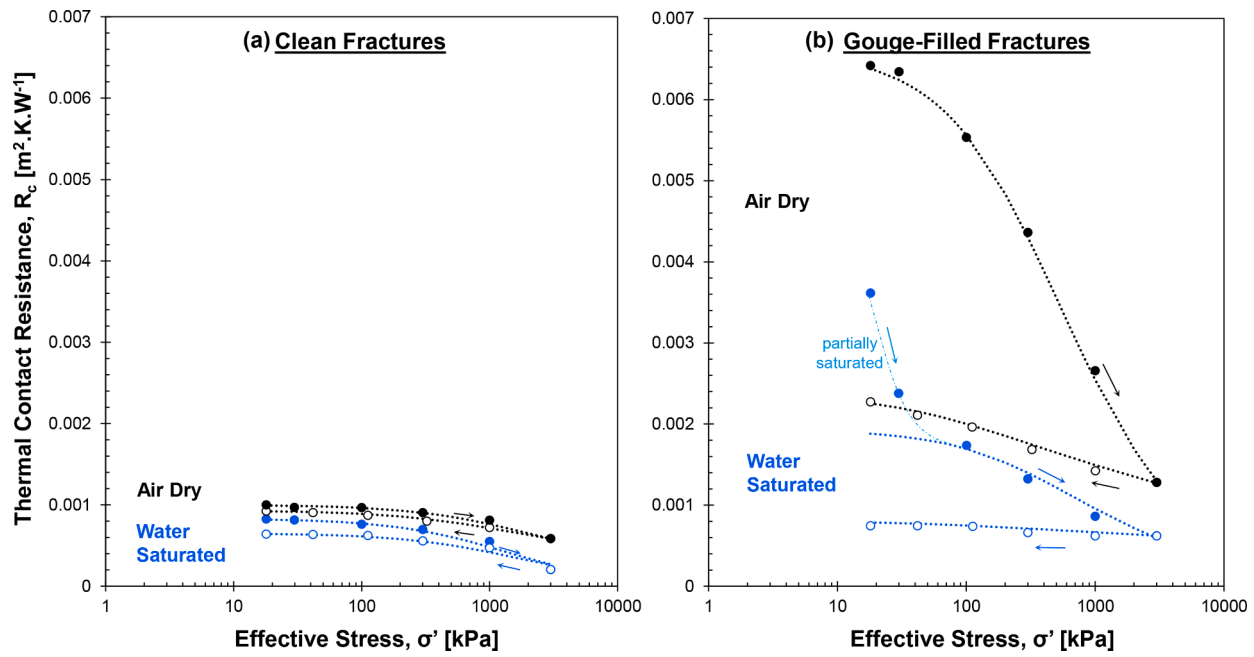


Figure 7. Thermal contact resistance under dry and water-saturated conditions during loading and unloading – Two-slab stack, i.e., single fracture. (a) Clean fractures. (b) Gouge-filled fractures. Lines show the fitted power function.

Table 1  
Thermal contact resistance – Values of the parameters in the power equation (Equation 3- Data in Figure 7).

			$R_{cl}$ [ $m^2 \cdot K \cdot W^{-1}$ ]	$\sigma_0$ [kPa]	$\beta$ [°]
Gouge-Filled	Air-Dry	Loading	0.0066	390	0.75
		Unloading	0.0024	50	0.15
	Water-Sat.	Loading	0.0019	350	0.52
		Unloading	0.0008	50	0.07
Clean	Air-Dry	Loading	0.0010	1000	0.39
		Unloading	0.0009	500	0.24
	Water-Sat.	Loading	0.00083	1200	0.90
		Unloading	0.00065	1200	0.73

Analogous to results for single fractures, the effective thermal conductivity of the rock mass improves (1) when fractures are clean rather than separated by gouge, i.e., fewer constrictions for heat flow, (2) under higher normal effective stress, i.e., higher true contact area, and (3) under wet conditions, i.e., enhanced heat transport at contacts. Furthermore, the presence of gouge increases stress sensitivity of the rock mass effective thermal conductivity and its hysteresis upon unloading.

The effective rock mass thermal conductivity can be estimated as a combination of the intact rock thermal conductivity  $k_m$  [ $W \cdot m^{-1} \cdot K^{-1}$ ] in series with the fracture thermal contact resistance  $R_c$  [ $m^2 \cdot K \cdot W^{-1}$ ] for a given fracture separation  $s$  [m]:

$$k_{eff} = \frac{1}{\frac{1}{k_m} + \frac{R_c}{s}} \quad (4)$$

Let's use this equation in combination with the contact resistance model (Equation 3 – Figure 7 – Parameters in Table 1) to calculate the effective thermal conductivity for all fractured rock masses tested in this study using a constant value for the intact limestone conductivity  $k_m = 2.83 \text{ W} \cdot \text{m}^{-1} \cdot \text{K}^{-1}$ . (Note: water can significantly improve thermal conduction in porous intact rocks as well – Zimmerman 1989, Alishaev et al. 2012, Li et al. 2020). The computed trends shown in Figure 8-b match closely with the experimental effective thermal conductivity trends.

Therefore, this methodology can be used to predict the effective

conductivity of rock masses from simple laboratory measurements of the matrix thermal conductivity  $k_m$  and fracture thermal contact resistance  $R_c$  under various stress and water saturation conditions.

## 5. Conclusions

Discontinuities in rocks – from microcracks to fractures and faults – couple effective thermal conductivity to stress, and fluid conditions.

The apparent thermal discontinuity across fractures arises from heat flow constriction at contacts, phonon scattering, and the low thermal conductivity of interstitial fluids. An increase in the effective stress reduces the fracture thermal contact resistance through the increase in true contact area, gouge and asperity crushing, and produced fines that fill the fracture space and contribute conduction pathways. These processes convey the high stress sensitivity and loading hysteresis to the fracture thermal contact resistance. A contact mechanics-inspired inverse power function adequately models the change in thermal contact resistance with stress.

Water reduces the thermal contact resistance by nearly 70% for clean and gouge-filled fractures. In particular, water fills the fracture interstices and forms menisci at mineral contacts that significantly improve heat conduction even in partially saturated rock masses.

Phenomena at the fracture scale strongly affect the rock mass thermal conductivity. In general, we anticipate that the thermal conductivity in more compressible rock masses will exhibit higher stress sensitivity.

The effective thermal conductivity computed by combining the contact resistance of a single fracture and the thermal conductivity of the intact block shows a close match to the effective thermal conductivity measured across the entire rock mass. Therefore, the rock mass effective thermal conductivity can be estimated from intact rock thermal conductivity measurements and the assessment of the thermal contact resistance of a single fracture in the lab. This approach overcomes inherent experimental difficulties associated with specimen size requirements when studying rock masses.

Data: All data are available in the manuscript and in the KAUST repository (with an assigned permanent DOI)

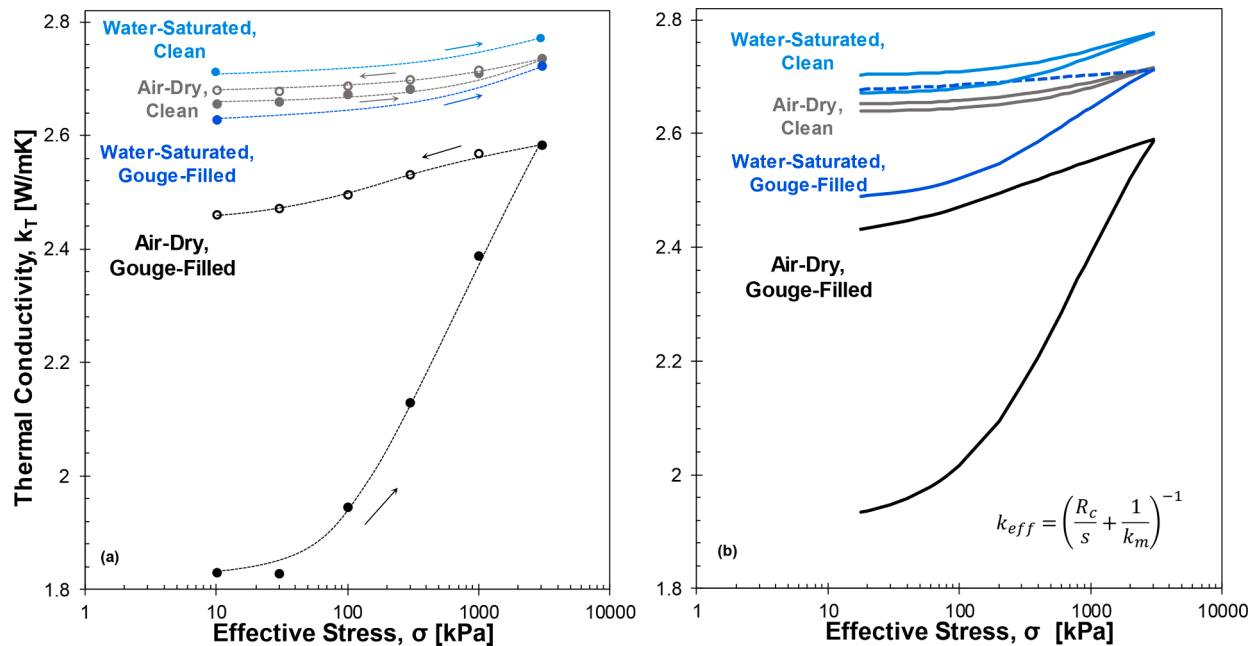


**Figure 8.** Effective thermal conductivity of fractured rock with clean and gouge-filled fractures under air-dry and water-saturated conditions – Five-slab stacks. (a) Experimental data. (b) Analytical predicted effective thermal conductivity computed from the thermal contact resistance of a fracture (data in Figure 6) and the thermal conductivity of the limestone slab.

#### CRediT authorship contribution statement

**A.V. Garcia:** Conceptualization, Methodology, Validation, Formal analysis, Investigation, Data curation, Writing – original draft, Writing – review & editing, Visualization. **J.C. Santamarina:** Conceptualization, Methodology, Validation, Formal analysis, Resources, Writing – original draft, Writing – review & editing, Supervision, Project administration, Funding acquisition.

#### Declaration of Competing Interest

The authors declare that they have no known competing financial interests or personal relationships that could have appeared to influence the work reported in this paper.

#### Acknowledgments

Support for this research was provided by the KAUST endowment at King Abdullah University of Science and Technology. Our gratitude extends to Gabrielle E. Abelskamp who edited the manuscript.

#### Supplementary materials

Supplementary material associated with this article can be found, in the online version, at doi:[10.1016/j.geothermics.2021.102113](https://doi.org/10.1016/j.geothermics.2021.102113).

#### References

- Abdulagatov, I.M., Emirov, S.N., Abdulagatova, Z.Z., Askerov, S.Y., 2006. Effect of pressure and temperature on the thermal conductivity of rocks. *Journal of Chemical & Engineering Data* 51 (1), 22–33.
- Abdulagatova, Z., Abdulagatov, I., Emirov, V., 2009. Effect of temperature and pressure on the thermal conductivity of sandstone. *International Journal of Rock Mechanics and Mining Sciences* 46 (6), 1055–1071.
- Abdulagatova, Z.Z., Abdulagatov, I.M., Emirov, S.N., 2010. Effect of pressure, temperature, and oil-saturation on the thermal conductivity of sandstone up to 250 MPa and 520 K. *Journal of Petroleum Science and Engineering* 73 (1–2), 141–155.
- Alishaev, M., Abdulagatov, I., Abdulagatova, Z., 2012. Effective thermal conductivity of fluid-saturated rocks: experiment and modeling. *Engineering Geology* 135, 24–39.
- Bär, K., Homuth, S., Rühaak, W., Schulte, D., Welsch, B., Sass, I., 2015. Coupled Renewable Energy Systems for Seasonal High Temperature Heat Storage via Medium

- Deep Borehole Heat Exchangers. In: Paper presented at the Proceedings World Geothermal Congress.
- Bridgman, P., 1924. The thermal conductivity and compressibility of several rocks under high pressures. *American Journal of Science* (38), 81–102.
- Brown, D.W., Duchane, D.V., Heiken, G., Hrisco, V.T., 2012. *Mining the earth's heat: hot dry rock geothermal energy*. Springer Science & Business Media.
- Clauser, C., Huenges, E., 1995. Thermal conductivity of rocks and minerals. *Rock physics and phase relations: a handbook of physical constants* 3, 105–126.
- Cooper, M., Mikic, B., Yovanovich, M., 1969. Thermal contact conductance. *International Journal of Heat and Mass Transfer* 12 (3), 279–300.
- Greenwood, J.A., Williamson, J.P., 1966. Contact of nominally flat surfaces. *Proceedings of the royal society of London. Series A. Mathematical and physical sciences* 295 (1442), 300–319.
- Hurtig, E., Brugger, H., 1970. Wärmeleitfähigkeitsmessungen unter einaxialem Druck. *Tectonophysics* 10 (1–3), 67–77.
- Jorand, R., Vogt, C., Marquart, G., Clauser, C., 2013. Effective thermal conductivity of heterogeneous rocks from laboratory experiments and numerical modeling. *Journal of Geophysical Research: Solid Earth* 118 (10), 5225–5235.
- Laloui, L., Nuth, M., Vulliet, L., 2006. Experimental and numerical investigations of the behaviour of a heat exchanger pile. *International Journal for Numerical and Analytical Methods in Geomechanics* 30 (8), 763–781.
- Li, Z.W., Zhang, Y.J., Gong, Y.H., Zhu, G.Q., 2020. Influences of mechanical damage and water saturation on the distributed thermal conductivity of granite. *Geothermics* 83, 101736.
- Lide, D.R., 2003. *Handbook of chemistry and physics* 84-th edition. CRC press.
- Madsen, F., 1998. Clay mineralogical investigations related to nuclear waste disposal. *Clay minerals* 33 (1), 109–129.
- Mikić, B., 1974. Thermal contact conductance; theoretical considerations. *International Journal of Heat and Mass Transfer* 17 (2), 205–214.
- Oldecop, L.A., Alonso, E.E., 2001. A model for rockfill compressibility. *Géotechnique* 51 (2), 127–139.
- Pasvanoğlu, S., 2020. Geochemistry and conceptual model of thermal waters from Erciş-Zilan Valley, Eastern Turkey. *Geothermics* 86, 101803.
- Popov, Y.A., Pribnow, D.F., Sass, J.H., Williams, C.F., Burkhardt, H., 1999. Characterization of rock thermal conductivity by high-resolution optical scanning. *Geothermics* 28 (2), 253–276.
- Prasher, R., Tong, T., Majumdar, A., 2007. Diffraction-limited phonon thermal conductance of nanoconstrictions. *Applied Physics Letters* 91 (14), 143119.
- Prasher, R.S., Phelan, P.E., 2006. Microscopic and macroscopic thermal contact resistances of pressed mechanical contacts. *Journal of Applied Physics* 100 (6), 063538.
- Stephens, G., Voight, B., 1982. Hydraulic fracturing theory for conditions of thermal stress. In: Paper presented at the International Journal of Rock Mechanics and Mining Sciences & Geomechanics Abstracts.
- Surma, F., Geraud, Y., 2003. Porosity and thermal conductivity of the Soultz-sous-Forêts granite. *Pure and Applied Geophysics* 160 (5–6), 1125–1136.
- Tsang, C.F., 2012. *Coupled processes associated with nuclear waste repositories*. Elsevier.
- Walsh, J., Decker, E., 1966. Effect of pressure and saturating fluid on the thermal conductivity of compact rock. *Journal of Geophysical Research* 71 (12), 3053–3061.

- Wang, Y., Dusseault, M.B., 2003. A coupled conductive–convective thermo-poroelastic solution and implications for wellbore stability. *Journal of Petroleum Science and Engineering* 38 (3-4), 187–198.
- Welsch, B., Rühhaak, W., Schulte, D.O., Baer, K., Sass, I., 2016. Characteristics of medium deep borehole thermal energy storage. *International Journal of Energy Research* 40 (13), 1855–1868.
- Yaşar, E., Erdoğan, Y., Güneçli, H., 2008. Determination of the thermal conductivity from physico-mechanical properties. *Bulletin of Engineering Geology and the Environment* 67 (2), 219–225.
- Yovanovich, M.M., 2005. Four decades of research on thermal contact, gap, and joint resistance in microelectronics. *IEEE transactions on components and packaging technologies* 28 (2), 182–206.
- Yun, T.S., Santamarina, J.C., 2008. Fundamental Study of Thermal Conduction in Dry Soils. *Granular Matter* 10 (3), 197–207.
- Zimmerman, R.W., 1989. Thermal conductivity of fluid-saturated rocks. *Journal of Petroleum Science and Engineering* 3 (3), 219–227.